RAA 2021 Vol. **21** No. **12**, 306(13pp) doi:10.1088/1674-4527/21/12/306

http://www.raa-journal.org *http://iopscience.iop.org/raa*

Research in
Astronomy and
Astrophysics

Spatially resolved properties of supernova host galaxies in SDSS-IV MaNGA

Hong-Xuan Zhang[1,2,3], Yan-Mei Chen[1,2,3], Yong Shi[1,2,3], Min Bao[1,2,3] and Xiao-Ling Yu[1,2,3]

[1] School of Astronomy and Space Science, Nanjing University, Nanjing 210093, China
[2] Key Laboratory of Modern Astronomy and Astrophysics (Nanjing University), Ministry of Education, Nanjing 210093, China
[3] Collaborative Innovation Center of Modern Astronomy and Space Exploration, Nanjing 210093, China; *chenym@nju.edu.cn*

Received 2021 July 22; accepted 2021 September 23

Abstract We crossmatch galaxies from Mapping Nearby Galaxies at Apache Point Observatory with the Open Supernova Catalog, obtaining a total of 132 SNe within MaNGA bundle. These 132 SNe can be classified into 67 Type Ia and 65 Type CC. We study the global and local properties of supernova host galaxies statistically. Type Ia SNe are distributed in both star-forming galaxies and quiescent galaxies, while Type CC SNe are all distributed along the star-forming main sequence. As the stellar mass increases, the Type Ia/CC number ratio increases. We find: (1) there is no obvious difference in the interaction possibilities and environments between Type Ia SN hosts and a control sample of galaxies with similar stellar mass and SFR distributions, except that Type Ia SNe tend to appear in galaxies which are more bulge-dominated than their controls. For Type CC SNe, there is no difference between their hosts and the control galaxies in galaxy morphology, interaction possibilities as well as environments; (2) compared to galaxy centers, the SN locations have smaller velocity dispersion, lower metallicity, and younger stellar population. This is a natural result of radius gradients for all these parameters. The SN location and its symmetrical position relative to the galaxy center, as well as regions with similar effective radii have very similar [Mg/Fe], gas-phase metallicity, gas velocity dispersion and stellar population age.

Key words: galaxies: general — galaxies: abundances — supernovae: general — techniques: spectroscopic

1 INTRODUCTION

Supernova (SN) explosion, as an important astrophysics process, can be classified into Type I and II according to the presence of hydrogen line or not in their spectra (Filippenko 1997). Type I Supernovae (SNe) are divided into Type Ia with Si 6510Å absorption line, Type Ib without Si but with He line, and Type Ic neither with Si or He line in the spectra (Hamuy et al. 2002). Type II SNe can be divided into Type IIP and Type IIL (Barbon et al. 1979) by light curves. Type IIP has a long plateau (∼90 days) after the curve reaches its peak (Rubin et al. 2016) while Type IIL shows a linear decline after the peak.

In another way, we can also classify SNe by their progenitors. The explosion of a progenitor star with stellar mass $> 8\ M_\odot$ is induced by the gravitational collapse and leaves a neutron star or black hole in the center (Arnett et al. 1989; Bethe et al. 1979). This is named as core collapse supernovae (CC SNe), which is corresponding to Type Ib/c and Type II SNe. Meanwhile, a star with stellar mass between 0.5∼8 $M_\odot$ will evolve into a degenerate carbon-oxygen (C/O) white dwarf (WD, Becker & Iben 1980) as its end. If the mass of the WD is larger than ∼1.44 $M_\odot$, thermonuclear reactions can ignite the center of the WD and lead to a great thermonuclear explosion which is named Type Ia SNe (Hoyle & Fowler 1960).

As a result, Type Ia SNe have been recognized as an important cosmological probe. Because of their stable peak luminosity, it is treated as the best standard candle up to date. It provides the evidence of accelerating expansion of the universe and the existence of dark energy (Perlmutter et al. 1999; Riess et al. 1998). However, there have been several studies showing that the peak luminosity of Type Ia SNe varies with host galaxies properties, which would lead to uncertainties in constraining cosmological models. At the early stage, these studies focused mainly on the global properties of host galaxies, and how the peak luminosity of Type Ia SNe depends on stellar masses (Sullivan et al.

2010), ages (Hamuy et al. 1995, 2000) and gas metallicities (Gallagher et al. 2005).

As these kinds of investigation went deeper and deeper, astronomers realized that the local environments should be important to properties of SNe. However, there was no large spatial resolved surveys by that time, the studies were focused on the locations where the supernova explodes (Anderson & James 2009; Galbany et al. 2012) since most galaxy properties have obvious radial gradients.

With the development of observation technology, the emergence of integral field unit (IFU) survey provides spatial resolved information of galaxies and makes it possible to construct a direct observation of properties at SN exploding location. Stanishev et al. (2012) compared local and global properties and environments of host galaxies of 6 Ia SNe and found no obvious difference in metallicity based on the Calar Alto Legacy Integral Field Area (CALIFA) survey. Galbany et al. (2014, 2016) expanded the sample size of SN host galaxies to 115. By the PMAS/PPAK Integral-field Supernova hosts Compilation (PISCO), Galbany et al. (2018) has enlarged the sample to 232 host galaxies with 272 SNe.

Zhou et al. (2019) compared properties of SN exploding locations with global properties of their host galaxies based on MaNGA data, including 4 Type Ia, 5 Type II and 2 unclassified SNe, and found that all of the SNe are exploded in metal-rich galaxies with $12 + \log(\mathrm{O/H}) > 8.5$ but showed small difference between local and global metallicity. In 2020, Zhou et al. revisited the same question and found similar results with a larger sample of 67 SNe.

We notice that most of the previous researches based on IFS observations do not take the radial gradients into account. However, the comparison between local and global properties could be influenced by radial gradients. In this work, we build a sample of 132 SNe with MaNGA observations of host galaxies, comparing the properties of SN location with different regions in the host galaxies.

The paper is organized as follows: in Section 2, we describe our sample selection criteria. Then we show the comparison results in aspects of both global and local properties in Section 3. The results and conclusions are shown in Sections 4 and 5. The cosmological parameters we use throughout this paper are $H_0 = 70\,\mathrm{km\ s^{-1}\ Mpc^{-1}}$, $\Omega_\mathrm{M} = 0.3$, and $\Omega_\Lambda = 0.7$.

2 OBSERVATIONS AND DATA REDUCTION

2.1 Mapping Nearby Galaxies at Apache Point Observatory

MaNGA (Bundy et al. 2015), as one of three major programs in Sloan Digital Sky Survey IV (Blanton et al. 2017), uses Apache Point Observatory's 2.5-meter telescope (Gunn et al. 2006) for observation. MaNGA launched in 2014 July, and was completed in early 2021, obtaining the largest spatial resolved galaxy sample so far (∼10,000 galaxies). In order to observe the distribution of the gas, stellar kinematics and stellar populations in galaxies of different sizes, the MaNGA IFUs include different sizes of fiber-bundles. Each cartridge includes $2\times\mathrm{N}_{19}$, $4\times\mathrm{N}_{37}$, $4\times\mathrm{N}_{61}$, $2\times\mathrm{N}_{91}$, $5\times\mathrm{N}_{127}$, altogether 17 different sizes of bundles as well as $12\times\mathrm{N}_7$ mini-bundle per cartridge for flux calibration (Drory et al. 2015; Yan et al. 2016). The two dual-channel BOSS spectrographs (Smee et al. 2013) provide a simultaneous wavelength range of 3600∼10300Å with a spectral resolution of R∼2000. As a result of 3 hours in typical integration time, the $r-$band signal-to-noise ratio (S/N) reaches 4∼8 at 23 mag arcsec^{-2}.

The target sample covers a range in redshift 0.01 ∼ 0.15 with a median redshift of 0.03. The stellar mass has a flat distribution in between $10^9 M_\odot$ to $10^{11} M_\odot$ for ensuring adequate sampling of stellar mass. The MaNGA galaxies are separated into two different subsamples: the primary sample includes more than 80% of all targets and covers to 1.5 effective radii (R_e) and the secondary sample to $2.5\mathrm{R}_e$.

The MaNGA data used in this work include observations of 8000 unique galaxies in MaNGA Product Launch-9 (MPL9). The raw data is reduced by Data Reduction Pipeline (DRP, Law et al. 2016) and then analyzed through the Data Analysis Pipeline (DAP, Westfall et al. 2019; Belfiore et al. 2019).

2.2 The Open Supernova Catalog

The Open Supernova Catalog (TOSC, Guillochon et al. 2017) is a website dedicated to collecting supernova data[1]. It has collected nearly 78,000 supernova and candidates till March 2021, most of which come from public supernova catalogs and projects, such as Asiago Supernova Catalog (ASC, Barbon et al. 1999), Caltech Core-Collapse program (CCCP, Gal-Yam et al. 2004), Cambridge Photometry Calibration Server (CPCS, Zieliński et al. 2019), etc. It also collects individual supernovae in published papers (e.g., Yaron & Gal-Yam 2012; Matheson et al. 2008; Silverman et al. 2012). This website provides basic parameters including SN name, type, position, redshift, and whether it contains X-ray and radio observations. Currently, about 20,000 supernovae in the catalog contain light curves, and about 10,000 contain spectra. This website has laid a solid foundation for the systematic researches of supernovae.

---

[1] `https://sne.space`

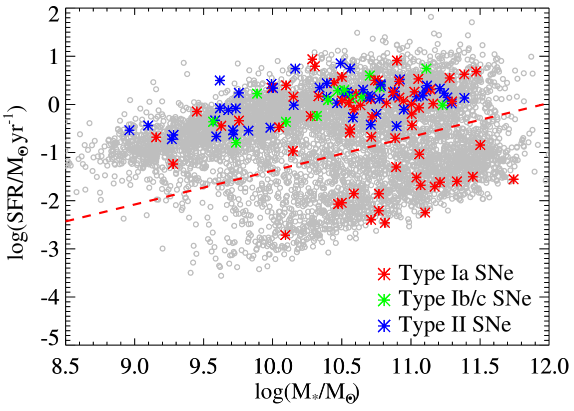

Fig. 1 The SFR vs. M_* diagram of Type Ia (*red asterisk*), Type Ib/c (*green asterisk*) and Type II SNe (*blue asterisk*), the grey circles in background are from MaNGA MPL9 and the red dash line is 2σ below the star forming main sequence.

2.3 Sample Selection and Data Analysis

At first, we crossmatch 8000 galaxies from MPL9 with 77951 SNe from TOSC with a tolerance radius of 3R$_e$ of the MaNGA galaxy and obtain 411 SN host galaxies. Meanwhile, there is a MaNGA ancillary program planned to observe host galaxies of 60 type Ia supernova (Accetta et al. 2021). In MPL9, 7 of these 60 targets have been observed and we find that three of them are included in our sample. We then exclude 188 SNe as well as their host galaxies from our sample since the type of these SNe is not clear. we also remove 47 SNe which are located outside the MaNGA bundles. The stellar mass and SFR are taken from MPA-JHU[2] catalog. The total stellar mass is estimated through the fitting of SDSS $ugriz$ 5-band SED (Kauffmann et al. 2003). The SFR is estimated from the luminosity of Hα emission line (Brinchmann et al. 2004). Finally we get a sample of 132 SNe, which includes 67 Type Ia and 65 Type CC SNe (8 Type Ib, 6 Type Ic and 51 Type II). The basic information of these SNe is listed in Table A.1.

MaNGA DAP (Westfall et al. 2019) fits the galaxy's spectrum based on MaStar Library (Yan et al. 2019) using pPXF spectrum processing software (Cappellari & Emsellem 2004). The DAP fits the stellar continuum and 21 nebular emission lines of main optical bands for each spaxel. The parameters extracted in this work are from the DAP named "SPX-MILESHC-MASTARHC" including nebular emission line fluxes ([N II]λ6584 & [S II]$\lambda\lambda$6717,6731), the spectral indices ([Mg/Fe] & Dn4000) and velocity dispersion of ionized gas ($\sigma_{\mathrm{H}\alpha}$), etc.

Figure 1 shows the distributions of Type Ia (red asterisk), Type Ib/c (green) and Type II (blue) SN host galaxies in SFR vs. M_* diagram. The grey circles represent MaNGA MPL9 galaxy sample, and the red dash line separates the star-forming main sequence with higher SFRs from quiescent galaxies. We can find that Type CC SNe (including Type Ib/c and Type II) are all located in the star-forming main sequence above the dash line, which corresponds to the fact that the progenitor of these SNe are all massive young stars and formed in star-forming region. Meanwhile, Type Ia SNe distribute in both blue and red galaxies because the progenitors of Ia SNe are all low-mass stars, which exist in both star-forming and quiescent galaxies. This result is consistent with Shao et al. (2014) that among their 902 SNe, Type CC SNe are most distributed in star forming galaxies and a small part in AGN and quiescent galaxies while Type Ia distributed in both types of galaxies.

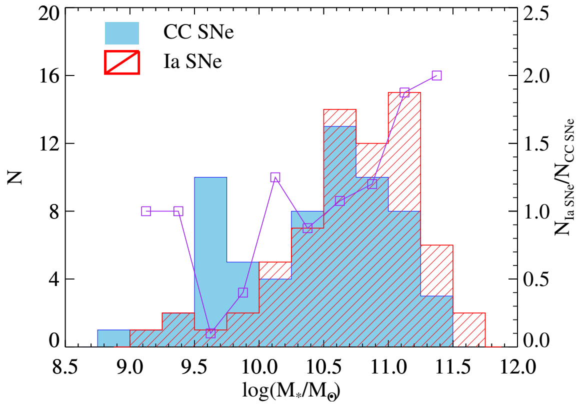

Fig. 2 The stellar mass distribution of Type Ia (*red*) and Type CC (*blue*) SN host galaxies. The purple open squares and solid line represent the Ia/CC SNe number ratio in each bin.

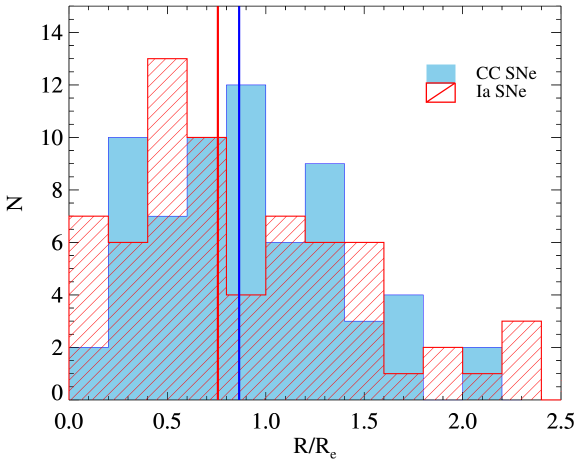

Fig. 3 The distribution of the SN position relative to the galaxy center in unit of R$_e$. Red histogram is for Type Ia and blue for Type CC SNe. Red and blue solid lines represent the median values.

Figure 2 shows the stellar mass distribution of Type Ia (red histogram) and Type CC (blue) SN host galaxies. The purple squares and line shows the ratio between the

---

[2] https://wwwmpa.mpa-garching.mpg.de/SDSS/DR7/

number of Type Ia and CC SNe. At $\log M_*/\mathrm{M}_\odot < 9.5$, the statistical uncertainty of number ratio is large due to that there are only 3 Type Ia and 4 CC SNe in this mass range. At $\log M_*/\mathrm{M}_\odot > 9.5$, the ratio increases quickly with stellar mass, consistent with the fact that the median stellar mass of Ia host galaxies is higher than Type CC host galaxies in Zhou et al. (2020).

In Figure 3, we show the distribution of the SN position relative to the galaxy center in unit of R_e. The red histogram represents Type Ia SNe, blue represents CC and the red and blue vertical lines represent the median values of Ia and CC SNe, respectively. The distribution of the two SN types shows no significant difference. The sharp decrease of SN number outside $1.5\mathrm{R}_e$ is due to the fact that only 20% of MaNGA bundles cover beyond $1.5\mathrm{R}_e$.

In order to compare the properties of SN host galaxies and non-SN host galaxies, we build a non-SN host galaxy control sample, which is closely matched in M_*, SFR and z. The specific selection method is shown in Equation (1).

$$\Delta s = \left|\frac{\Delta\log M_*}{0.1}\right| + \left|\frac{\Delta\log\mathrm{SFR}}{0.2}\right| + \left|\frac{\Delta z}{0.001}\right| \tag{1}$$

We choose galaxy with smallest Δs as SN control where $\Delta\log M_*$ represents the stellar mass difference between the SN host galaxy and its control, $\Delta\log\mathrm{SFR}$ and Δz represent the SFR and redshift difference, respectively. The motivation of choosing these three parameters to build control sample is the following: (i) as one of the fundamental parameters, stellar mass correlates strongly with many other parameters of galaxies such as metallicity and SFR; (ii) the SFR is a major factor of SN explosions especially for Type CC SNe, a high SFR represents a high SN explosion rate; (iii) a similar redshift distribution is required to avoid the influence of any evolutionary effects. Figure 4 shows the distributions of SN host galaxies and the control sample in SFR vs. M_* diagram. The blue and cyan solid squares correspond to Type Ia and Type CC SN host galaxies. The red and orange open triangles correspond to the control galaxies of Type Ia and Type CC, respectively. The top and right panels show the histograms of M_* and SFR for the SN sample (blue) and the control sample (red). It is clear that the SN sample and the control sample have similar M_* and SFR distributions.

3 RESULTS

In this section, we compare the morphology, interaction possibility parameter and environment of the SN host galaxies and control sample, trying to understand the correlation between these properties and SN explosions. Thanks to the large IFU sample provided by MaNGA survey, we can compare the properties of the local region of SN explosions and other locations within the galaxy, investigating the connection between the SN explosions and the properties of their host galaxies.

3.1 The Global Properties of SN Host Galaxies

We use Sèrsic index n to characterize the morphology of galaxies (Sérsic 1963; Sersic 1968). The surface brightness of a galaxy can be fitted by Sèrsic profile:

$$I(R) = I_0 \exp[-\beta_n (\frac{R}{R_e})^{1/n}] \tag{2}$$

where I_0 is the central surface brightness of the galaxy and the parameter n in Equation (2) represents the Sèrsic index. $n = 2$ is generally used as the threshold between disk galaxies ($n < 2$) and elliptical galaxies ($n > 2$). We take n of our sample from PyMorph[3] (Fischer et al. 2019) in MaNGA data release 15 (DR15). MaNGA Morphology Deep Learning[4] (Domínguez Sánchez et al. 2018) provides a parameter named P_merg for DR15, which represents the likelihood that the galaxy has recently experienced interactions by optical images (Willett et al. 2013). The environment parameters d_1st and N_neigh are taken from GEMA-VAC[5] (Goddard et al. 2017), where d_1st is the projection distance between the target galaxy and the nearest neighbour with r-band magnitude $m_r < 17.7$. N_neigh is the total number of neighbor galaxies with $m_\mathrm{r} < 17.7$, a line-of-sight velocity to the target galaxy within $\pm 500\,\mathrm{km\,s^{-1}}$, the projection distance within 1Mpc.

Figure 5 shows the distribution of morphology, merging possibility and environmental parameters of Type Ia SN host galaxies and the control sample. The blue histogram represents the SN sample and the red represents the control sample. The vertical lines of different colors correspond to the median values of different distributions. In Figure 5(a), the median value of Sèrsic index of Ia SN host galaxies is higher than the control sample with $n = 3.6$ for SN sample and $n = 2.6$ for controls, indicating that Type Ia SNe tends to explode in galaxies which are more bulge-dominated. Figure 5(b) shows that Type Ia hosts and their controls have very similar merging possibility (P_merg) distributions, indicating there is no obvious connection between merger/interaction and SN explosion. For environments, we find both d_1st and N_neigh shown in Figure 5(c) & (d) reflect similar distributions and median values, indicating a weak/no correlation between

---

[3] https://www.sdss.org/dr15/data_access/value-added-catalogs/?vac_id=manga-pymorph-dr15-photometric-catalog

[4] https://www.sdss.org/dr15/data_access/value-added-catalogs/?vac_id=manga-morphology-deep-learning-dr15-catalog

[5] https://www.sdss.org/dr15/data_access/value-added-catalogs/?vac_id=gema-vac-galaxy-environment-for-manga-value-added-catalog

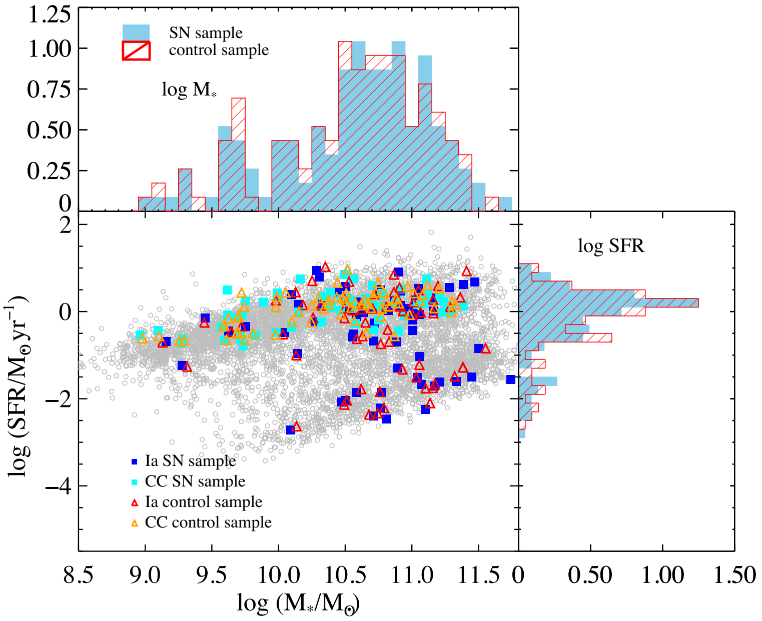

Fig. 4 The SFR vs. M_* diagram of SN sample (blue and cyan solid square for Type Ia and Type CC sample) and control sample (*red and orange open triangle* for Type Ia and Type CC sample) and MaNGA MPL9 sample (*grey open circles*), the top and right panels show histograms of M_* and SFR, respectively. In each panel, the histogram filled with blue color is for the SN sample and that filled with red strip lines is for the control sample.

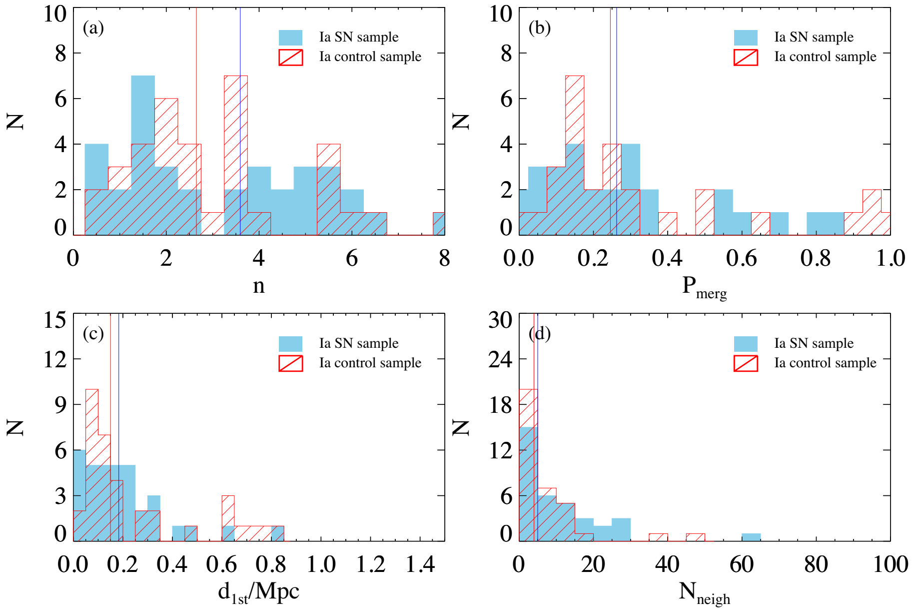

Fig. 5 The distribution of four parameters of Type Ia SN host galaxies (*blue*) and their control samples (*red*). **(a)** Sèrsic index n; **(b)** merging possibility $P_{\rm merg}$; **(c)** $d_{\rm 1st}$ /Mpc: the projection distance of the nearest neighbor galaxy with m_r < 17.7; **(d)** $N_{\rm neigh}$: the total number of neighbor galaxies with m_r < 17.7, a line-of-sight velocity to the target galaxy within ±500 km s^{-1}, the projection distance within 1Mpc. The solid vertical lines represent the median value of different samples.

triggering of Type Ia SNe and the environments of their host galaxies.

Similar to Figure 5, Figure 6 compared the Type CC SN host galaxies and their control sample, in which blue histograms represent Type CC hosts and the red represent the control galaxies, the two vertical lines of blue and red colors correspond to the median value of SN hosts and controls, respectively. Again, no difference is shown in Figure 6 indicating that there is no preference of SN

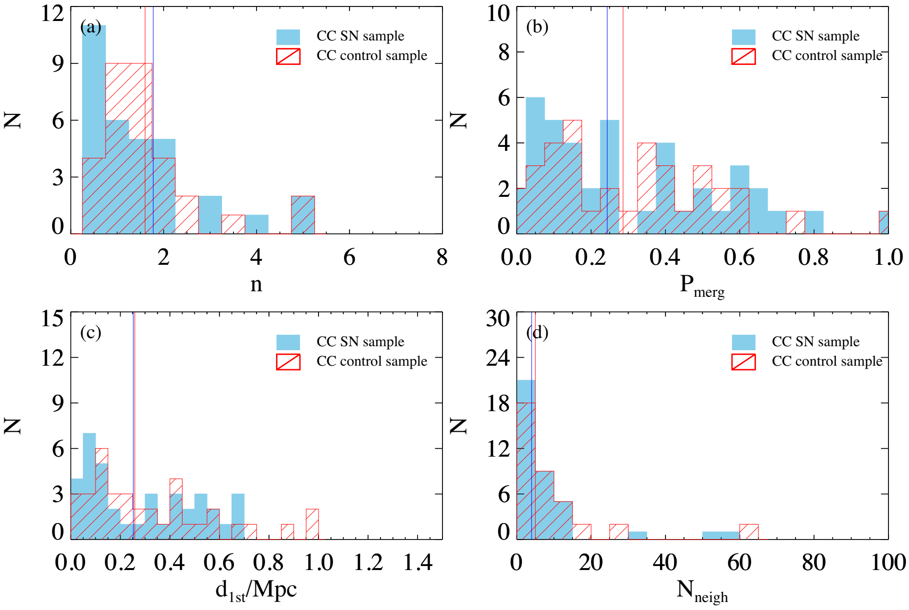

Fig. 6 Similar to the Fig. 5, but for Type CC SN host galaxies and their control samples.

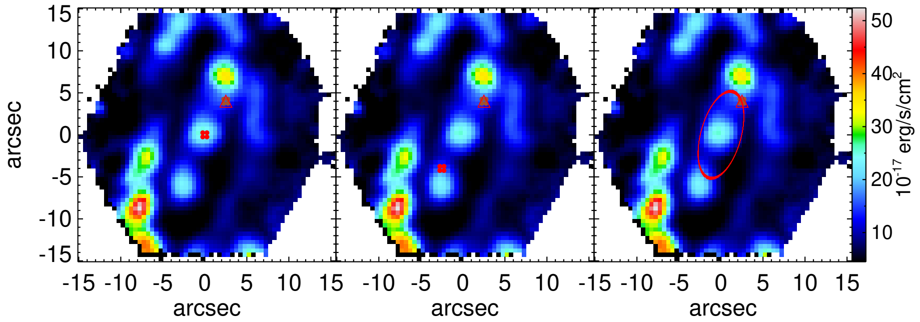

Fig. 7 An example of Hα flux map in MaNGA survey (MaNGAID: 1–115365). We mark the SN explosion location (*red open triangle* in all panels) and spaxels selected as SN explosion location (brown dots in all panels), the galaxy central region (*red dots* in left panel), the symmetric position of SN explosion region relative to the center of the galaxy (*red dots* in middle panel) and the annulus area with same effective radius as the SN explosion location (*red ellipse* in right panel).

explosion on the morphology, interaction and surrounding environment of their host galaxies.

3.2 The Local Properties of SN Host Galaxies

To further explore the local properties of the position where SNe explode, and to understand the speciality of the local environment, we select four regions in a galaxy for the comparison of galaxy properties: (i) the SN location: we select spaxels within 1″ radius from MaNGA data around the SN location, taking the median value of the physical parameters as the local properties of SN regions; (ii) the galaxy center: we select the spaxels within 1″ of galaxy center, taking the median parameters as the local properties of galaxy center region; (iii) the symmetric region of SN location relative to the center of the galaxy: we select the spaxels with 1″ of the symmetric region of SN location relative to the center of the galaxy, taking the median parameters as the local properties; (iv) the annulus area with same effective radius as the SN location: we select the spaxels at the annulus with the same effective radius as the SN position with a width ±0.05R$_e$, and take the median value as the properties of the annulus.

Figure 7 is an example of Hα flux map of SN host (MaNGAID: 1-115365). The SN location is marked as red triangles in each panel, the four brown dots are selected spaxels of the SN position. In the left panel, the four red dots in the middle represent the spaxels selected as galaxy center. At the bottom-left of the middle panel, the four red dots represent the data selected as symmetric position of SN explosion region relative to the center of the host galaxy. The red ellipse shown in right panel represents the data selected as the annulus area with same effective radius as the SN explosion location. The SN exploded in this galaxy is SN2007cn, which is classified as Type Ia.

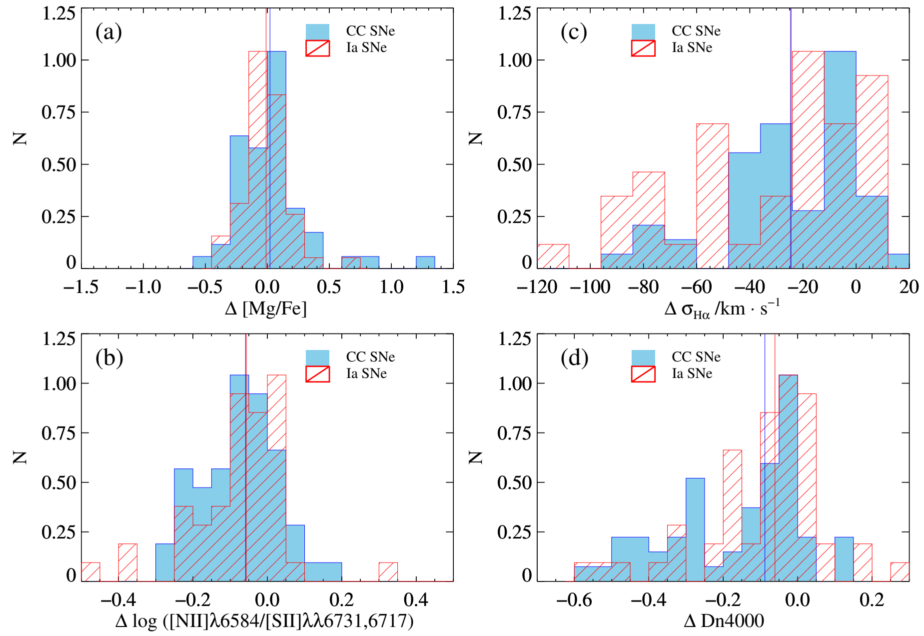

Fig. 8 The distribution of the difference in [Mg/Fe] (a) [N II]λ6584/[S II]$\lambda\lambda$6717,6731 (b) $\sigma_{\mathrm{H}\alpha}$ (c) Dn4000 (d) between SN position and the galaxy center. The red shaded histograms are for Type Ia SNe and blue for Type CC SNe. The vertical lines of different colors correspond to the median value of each distribution.

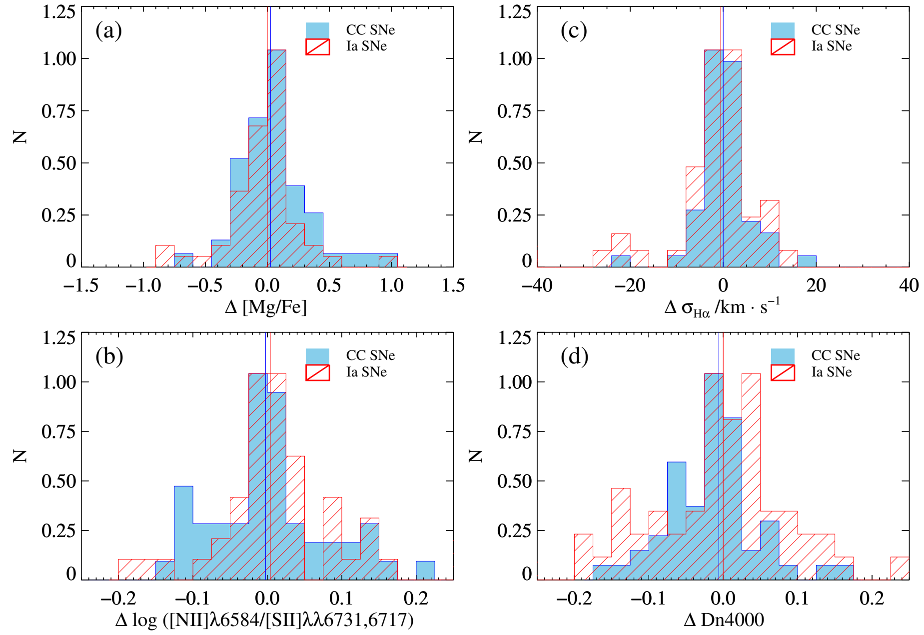

Fig. 9 Similar to the Fig. 8. But for the differences in [Mg/Fe], [N II]λ6584/[S II]$\lambda\lambda$6717,6731, $\sigma_{\mathrm{H}\alpha}$, D$n$4000 between the SN location and the symmetric region relative to the galaxy center.

We chose four parameters for comparison in this section: (i) we use [Mg/Fe] to roughly represent the star formation history. The magnesium element is an α-process element, and the synthesis of the α element mainly comes from the explosion of Type CC SNe whose progenitors have a relatively short lifetime (about 1$\sim$10 Myr); Meanwhile most of the iron is formed from the explosion of Type Ia SNe whose progenitors are low mass star with a long lifetime. Due to the different time scale of their formation, the ratio [Mg/Fe] is a good tracer of the star formation history (Thomas et al. 2010). The definition of [Mg/Fe] is:

$$[\mathrm{Mg/Fe}] = \mathrm{Mgb}/(0.5 \times \mathrm{Fe}\lambda5270 + 0.5 \times \mathrm{Fe}\lambda5335) \tag{3}$$

where the parameter Mgb, Feλ5270 and Feλ5335 are Lick indexes (Worthey 1994) included in MaNGA DAP;

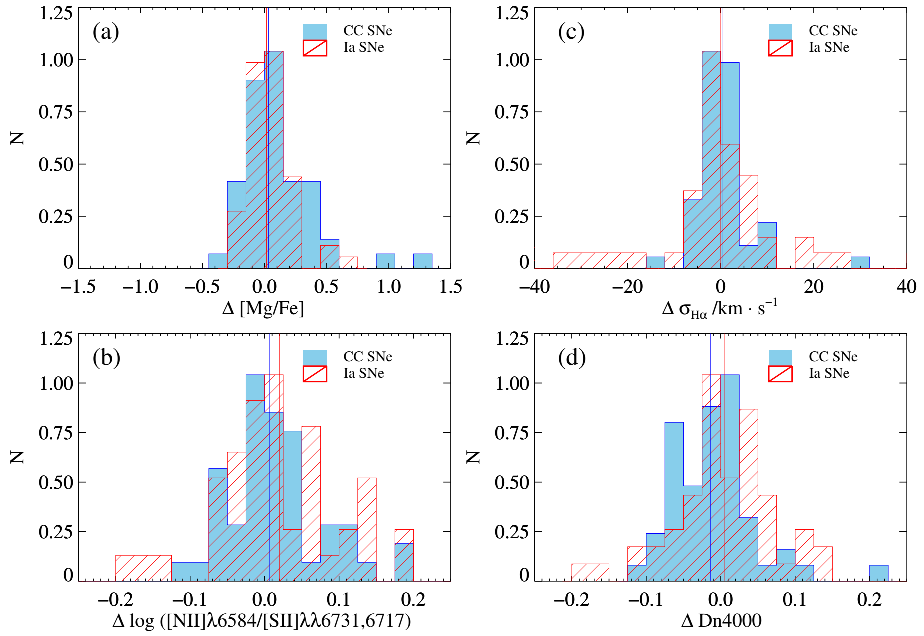

Fig. 10 Similar to the Fig. 8. But for the differences in [Mg/Fe], [N II]λ6584/[S II]$\lambda\lambda$6717,6731, $\sigma_{\rm H\alpha}$, Dn4000 between the SN location and the annulus region with the same effective radius as SN position.

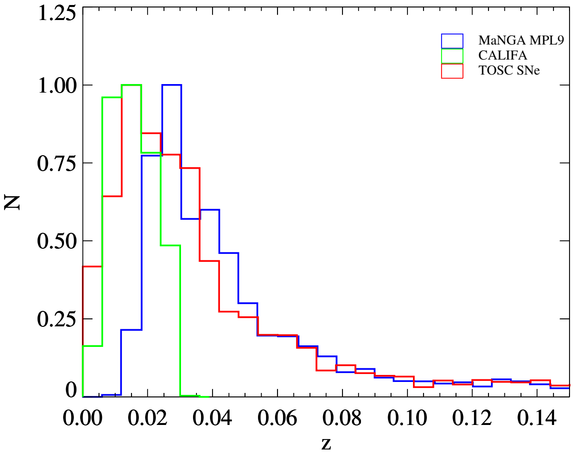

Fig. 11 Redshift distribution of MaNGA MPL9 sample (*blue*), CALIFA sample (*green*) and TOSC SN sample (*red*). The peaks of all the distributions are set to 1.

(ii) we use [N II]λ6584/[S II]$\lambda\lambda$6717,6731 (Kewley & Dopita 2002; Dopita et al. 2013) to characterize the gas-phase metallicity. We do not use metallicity indicators such as R_{23} in this work since most of the spaxels in SN (especially type Ia) host galaxies are not star forming, the traditional gas-phase metallicity indicator becomes invalid. But [N II]λ6584/[S II]$\lambda\lambda$6717,6731 could overcome this problem in that nitrogen is a secondary α-process element, and sulfur is a primary nuclear synthesis element. Although [N II]λ6584/[S II]$\lambda\lambda$6717,6731 is an approximation of N/O, at metallicity 12+log (O/H) $>$ 8.0, it has a good correlation with the O/H abundance (Dopita et al. 2016; Kashino et al. 2016). Since [N II]λ6584 and [S II]$\lambda\lambda$6717,6731 have similar wavelengths, the reddening effects could also be neglected; (iii) we use ionized gas velocity dispersion $\sigma_{\rm H\alpha}$ to explore the influence of SN explosions on gas kinematics; (iv) Dn4000 is a good indicator of stellar population age. It is defined by Balogh et al. (1999) as the ratio of average flux density between 3850Å$\sim$3950Å and 4000Å$\sim$4100Å.

Figure 8 shows distributions of the difference in [Mg/Fe], [N II]λ6584/[S II]$\lambda\lambda$6717,6731, $\sigma_{\rm H\alpha}$, Dn4000 between the SN exploding location and the galaxy center. The red shaded histograms are for Type Ia SNe and blue for Type CC SNe. A positive difference means the parameter at SN exploding location has higher value than that of galaxy center. The vertical lines of different colors correspond to the median value of each distribution. Figure 8(a) shows the difference in [Mg/Fe]. The median value of both distributions are approaching 0 ($-$0.01 for Type Ia SNe and 0.02 for Type CC SNe), implying that there is no significant difference in star formation history between the SN position and the galaxy center. While in Figure 8(b), we find that both Type Ia and Type CC SNe show obvious metallicity differences between the SN position and the galaxy center. The metallicity at SN position is lower than the galaxy center by $\sim$0.1 dex. Considering that the metallicity gradient of local star forming galaxies is typically $\sim$0.1 dex/R$_e$ (Schaefer et al. 2020), and the median value of SN position relative to the galaxy center is 0.8$\sim$0.9R$_e$ as shown in Figure 3, this metallicity difference observed in Figure 8(b) can be explained as a natural result of galaxy metallicity gradient. Figure 8(c) shows the difference in gas velocity dispersion. The median values of the differences in the Type Ia and Type CC SNe are -18km s^{-1} and -16km s^{-1}, indicating that the gas velocity dispersion at the SN position is smaller than that of the galaxy center. This difference is mainly due to the larger contribution of the bulge at the galaxy center. The SN position locates mainly at the outer regions of galaxies where the contribution of the galaxy disk increases, and therefore has a lower velocity dispersion than the central area. Figure 8(d) is the difference in Dn4000. A negative value in ΔDn4000 indicates that the stellar populations at SN position is younger than the galaxy center. SN position (with lower Dn4000) is younger than the galaxy center. This is also a direct result of the stellar population gradient in a normal galaxy with the inside-out growth model (Fall & Efstathiou 1980; Mo et al. 1998; Somerville et al. 2008). In brief, the comparison of the parameters in the SN explosion position and the galaxy center shows that the observed differences can be naturally explained by the radial gradient of the parameters. It does not show either the special features of the SN position or the influence of a single SN explosion on the local physical properties of the host galaxy.

In order to eliminate the influence of radial gradient, we compare the difference in the four parameters between SN location and its symmetrical region relative to the galaxy center. Statistically, the symmetrical region can be treated as a progenitor of SN location. The results are shown in Figure 9. Similar to Figure 8, the red shaded histograms are for Type Ia SNe and blue for Type CC SNe. The two vertical lines in each panel show the median value of the distributions with the same color. It is clear that the median values are all close to 0, indicating that there is no significant difference between SN location and the symmetrical region. Considering that the symmetrical region could represent the state of the SN location before explosion, this result suggests: (i) the properties of the SN location do not show any particularities; (ii) the impact of a single SN explosion is not strong enough to be observed at the explosion region, or (iii) the spatial resolution is not higher enough to resolve the region that a single SN can affect. The typical spatial resolution of MaNGA is $\sim$1.2 kpc considering a $2''$ fiber size at a median redshift of z $\sim$0.03. We are looking forward to higher spatial resolution IFU observations for further research.

Currently, the definition of symmetrical region covers only 3$\sim$4 spaxels, for which the physical properties could be influenced by substructures. Thus we further compare the average properties of SN location and elliptical annulus with the same effective radius as SN position. Similar to Figure 8, Figure 10 shows the distributions of difference between the median value of annulus region and the SN position in [Mg/Fe], $\sigma_{\mathrm{H}\alpha}$, [N II]$\lambda$6584/[S II]$\lambda\lambda$6717,6731 and D$n$4000. We find the difference of these parameters also has a value nearly zero, which again points to the result that the properties of SN location is similar to regions at the same effective radii. This result is consistent with Galbany et al. (2014, 2016) which found that the SFR and metallicity of the SN location are almost the same as that of the global properties of the galaxy based on the CALIFA survey.

4 DISCUSSION

4.1 Sample Size

In this work, we find 132 SNe with classification within the MaNGA bundle size from 8000 unique MaNGA galaxies, corresponds to $\sim$2% SN fraction. However, Galbany et al. (2016) found a SN fraction of $\sim$14% (= 132/939) from CALIFA survey. To understand the large difference in SN fraction, we explore the redshift distribution of MaNGA MPL9 (blue), CALIFA (green), and TOSC (red) samples in Figure 11. We find that the redshift of the CALIFA sample is mainly distributed at a redshift smaller than 0.03, and peaks $\sim$0.015. The redshift coverage of MaNGA is 0.01$\sim$0.15 and peaks at $\sim$0.03 with very few galaxies at z <0.015. There are 10,633 SNe in TOSC which has a clear SN type classification and a specific host galaxy. The peak of their host galaxy redshift distribution is around 0.015, similar to CALIFA. The large difference in SN fraction can be easily understood by the different redshift distributions: galaxy sample from CALIFA survey has similar redshift distribution as the SN host galaxies, while MaNGA galaxies are located at higher redshifts. The lower SN fraction is due to this redshift difference between MaNGA galaxy sample and SN hosts. This result is totally consistent with Zhou et al. (2019) who found a SN fraction of 1% (= 11/1390) in early MaNGA data release.

4.2 The Stellar Mass and Morphology of SN Host Galaxies

In this work, we study the distribution of supernova host galaxies on SFR vs. stellar mass relation, and find that the Type CC SN host galaxies are distributed in the star-forming main sequence, while Type Ia SNe are distributed in both star-forming galaxies and quiescent galaxies. This is consistent with the result of Shao et al. (2014) who found CC SNe mostly lie in star-forming galaxies and Ia SNe lie in star-forming, AGN, weak emission-line galaxies as well as absorption-line galaxies. Meanwhile, the increasing of the Type Ia/CC number ratio with stellar mass in this work suggests that Type Ia SNe tend to explode in galaxies with higher masses, which is in line with the result of Zhou et al. (2020).

We compare the global properties of SN host galaxies and control sample, finding that there is no obvious difference in galaxy interactions and surrounding environments. The Sèrsic index of Type Ia SN host galaxies is slightly higher than that of their control sample, indicating that Type Ia supernovae are more likely to explode in galaxies that are more bulge-dominated. However, Mannucci et al. (2005) found that the SN explosion rate is ∼20 times higher in spiral galaxies than that of elliptical galaxies. This result, at first sight, is in conflict with our result. Actually, this difference is due to that we are comparing the Type Ia hosts and their control galaxies with similar stellar mass and SFR, while Mannucci et al. (2005) compared SN explosion rate in spiral and elliptical galaxies. In Figure 1, we can find that there are 48 Type Ia SNe in star forming main sequence, and 19 Ia SNe locate in quiescent sequence below the red dashed line, indicating the Type Ia SN explosion rate is higher for star forming main sequence galaxies, which is in consistent with Mannucci et al. (2005) qualitatively.

5 CONCLUSIONS

In this paper, we crossmatch galaxies from MaNGA MPL9 to SNe from TOSC, obtaining a total of 132 SNe with classifications within MaNGA bundle. These 132 SNe can be classified into 67 Type Ia and 65 Type CC, where Type CC includes Type Ib, Ic, and Type II SNe. Type Ia SNe are distributed in both star-forming galaxies and quiescent galaxies, while Type CC SNe are all distributed along the star-forming main sequence. As the stellar mass increases, the Type Ia/CC number ratio also increases. Our conclusions are summarized as follows:

1. About the global properties of SN host galaxies, we find that there is no obvious difference in the interaction possibilities and environments between Type Ia SN hosts and a control sample of galaxies with similar stellar mass and SFR distributions, except that Type Ia SNe tend to appear in galaxies which are more bulge-dominated than their controls. For Type CC SNe, there is no difference between their host and the control galaxies in galaxy morphology, interaction possibility as well as environments. These results indicate the SN explosion rate is not depending on galaxy interactions and environments.
2. About the local properties, we find the SN locations with smaller velocity dispersion, lower metallicity, and younger stellar population than galaxy centers. This is a result of radial gradients of all these parameters. The comparison of physical properties ([Mg/Fe], [N II]λ6584/[S II]$\lambda\lambda$6717,6731, $\sigma_{\rm H\alpha}$ and Dn4000) between SN locations with the symmetric regions relative to galaxy centers and elliptical annulus with similar effective radii as SN location finds no obvious difference, indicating either there is no particularity in the properties at SN location or the scale that a single SN explosion can influence is much smaller than kpc, the typical resolution of MaNGA.

Acknowledgements We thank Yongyun Chen, Jianhang Chen and Songlin Li for very constructive comments in our work. Y. C acknowledges support from the National Key R&D Program of China (No. 2017YFA0402700), the National Natural Science Foundation of China (NSFC grants 11573013, 11733002, 11922302).

Funding for the Sloan Digital Sky Survey IV has been provided by the Alfred P. Sloan Foundation, the U.S. Department of Energy Office of Science, and the Participating Institutions. SDSS-IV acknowledges support and resources from the Center for High-Performance Computing at the University of Utah. The SDSS web site is www.sdss.org.

SDSS-IV is managed by the Astrophysical Research Consortium for the Participating Institutions of the SDSS Collaboration including the Brazilian Participation Group, the Carnegie Institution for Science, Carnegie Mellon University, the Chilean Participation Group, the French Participation Group, Harvard-Smithsonian Center for Astrophysics, Instituto de Astrofísica de Canarias, The Johns Hopkins University, Kavli Institute for the Physics and Mathematics of the Universe (IPMU) / University of Tokyo, Lawrence Berkeley National Laboratory, Leibniz Institut für Astrophysik Potsdam (AIP), Max-Planck-Institut für Astronomie (MPIA Heidelberg), Max-Planck-Institut für Astrophysik (MPA Garching), Max-Planck-Institut für Extraterrestrische Physik (MPE), National Astronomical Observatories of China, New Mexico State University, New York University, University of Notre Dame, Observatário Nacional / MCTI, The Ohio State University, Pennsylvania State University, Shanghai Astronomical Observatory, United Kingdom Participation Group, Universidad Nacional Autónoma de México, University of Arizona, University of Colorado Boulder, University of Oxford, University of Portsmouth, University of Utah, University of Virginia, University of Washington, University of Wisconsin, Vanderbilt University, and Yale University.

Appendix A:

References

Abdurró'uf, Accetta, K., Aerts, C., Silva, A. V., et al. 2021, arXiv:2112.02026

Anderson, J. P., & James, P. A. 2009, MNRAS, 399, 559

Arnett, W. D., Bahcall, J. N., Kirshner, R. P., & Woosley, S. E. 1989, ARA&A, 27, 629

Table A.1 Basic information for SN sample. The plate-ifudsgn column refers to the SN host galaxy observed in MaNGA.

SN Name	plate-ifudsgn	SN R.A.	SN Dec.	SN Type	redshift
SN2010ee	7495–12702	205.074951	26.353306	II	0.028401
SN2017frb	7815–3702	317.903473	11.497245	Ia	0.029382
SN2007cn	7979–12701	333.482452	13.756639	Ia	0.025379
SN2017jcu	8083–12704	50.695415	0.148083	II	0.022831
SN2007R	8138–12704	116.656372	44.789471	Ia	0.030805
SN2019smv	8258–3701	165.569458	44.334660	II	0.024607
SN2012hj	8257–12704	166.829956	46.379501	Ia	0.024578
SN2018hfc	8257–12701	165.494095	45.227539	II	0.019996
SN2018ats	8453–3701	153.234543	46.418091	Ia	0.038213
SN2012al	8453–12702	151.548370	47.294613	II	0.038107
SN2010D	8452–12705	157.934494	46.668056	II	0.024944
SN2018aex	8448–6102	165.189087	22.287500	II	0.022903
PTF11bui	8465–12705	198.235001	47.453472	Ia	0.028138
SN2019cvz	8484–12705	247.725021	46.588387	II	0.018346
SN2019gqd	8312–12703	247.208862	39.834347	Ic	0.035850
SN2020abla	8312–3704	247.164597	39.521030	Ia	0.025177
SN2015cq	8550–9101	247.410828	40.236111	II	0.028330
SN2005bp	7957–12704	257.430084	36.418915	II	0.027672
PTF09sh	8314–6101	243.492004	39.532806	II	0.037690
SN2008ev	8314–12701	240.758713	39.645611	II	0.030927
SN2000cs	8604–12701	245.884338	39.124748	II	0.035039
SN1999cb	8604–9102	246.451706	40.342335	Ia	0.029039
SN2018aej	8315–12704	236.095871	39.558094	Ia	0.047934
PS15aot	8603–6101	247.159836	39.548668	Ia	0.031176
SN2020mnv	8601–9101	250.182632	40.414482	Ia	0.025886
SN2011cc	8588–6101	248.455994	39.263527	II	0.031761
ASASSN-15ns	8588–6102	250.116745	39.320221	Ia	0.030079
SN2019eho	8615–9102	321.472076	0.414669	Ia	0.031740
SN2017fel	8616–12702	322.305756	–0.294703	Ia	0.030537
PTF12izc	8655–3702	355.893219	0.568667	Ia	0.082650
SN2015co	7960–12705	258.650543	30.735666	II	0.029594
SN2020jck	7968–12701	322.948822	–1.039164	Ia	0.051547
SN2010dl	7968–9102	323.754028	–0.513278	Ia	0.030156
SN2004I	8078–12701	40.880123	0.308528	II	0.026670
PTF12iiq	8078–6102	42.532333	–0.265111	Ia	0.029084
SN2019omi	8086–9102	57.249107	0.926919	Ia	0.035788
LSQ12fnt	8155–12701	53.172501	–1.186389	Ic	0.030451
SN2017ixz	8147–12701	116.762627	26.773825	II	0.023592
SN2017ckx	8145–1902	117.045876	28.230289	Ia	0.027158
SN2017cfq	8149–9102	120.980026	26.520203	II	0.021748
SN2020cvy	8149–3704	120.205307	27.498581	II	0.017345
SN2019abu	8084–12702	50.536613	–0.840061	II	0.036459
SN2018ddh	8262–6104	184.683502	44.781975	Ia	0.038341
SN2021drc	8450–6103	171.954544	21.386717	Ia	0.040623
SN2021efd	8450–9101	171.103043	23.649530	Ib	0.027756
ASASSN-15pn	8158–1901	60.859665	–5.492028	Ia	0.038357
LSQ12hxg	8158–9102	62.947582	–5.919028	II	0.038794
AT2017boa	8547–12701	217.631790	52.704327	Ia	0.044881
SN2002aw	8978–6102	249.371078	40.880638	Ia	0.026385
SN2020dow	8987–9102	137.983322	27.900387	Ia	0.047433
SN2018btb	8945–9102	173.616257	46.362530	Ia	0.033842
SN2020acfp	8945–12701	171.894165	47.379429	Ia	0.032730
SN1998cs	9029–12701	247.663422	41.215111	Ia	0.032463
SN2002cg	9029–12702	247.251999	41.283443	Ic	0.031887
SN2004ct	9041–9102	235.940628	28.416529	Ia	0.032751
SN2017dgs	9041–12702	236.389847	30.145430	II	0.031628
SDSS1684-53239-484	9027–1901	245.686615	32.659184	II	0.040998
SN2012fj	9027–12701	243.936920	31.963249	II	0.031547
SN2002ci	9027–9101	243.908127	31.321501	Ia	0.022198
SN2005bk	9036–9102	240.570999	42.915359	Ic	0.024435
PSN-J12565170+2629167	8951–12705	194.215424	26.487972	Ib	0.025364
SN2017cxz	8625–9101	259.832428	57.898834	Ib	0.028949
SDSS-II-SN-20130	7964–12704	316.558014	0.098017	II	0.050593
SN2019abp	9050–6102	245.860565	22.486141	II	0.037521
SN2007gl	8080–12705	47.888500	–0.746412	Ib	0.028230
SN2018jfp	8080–12703	49.484486	–0.169706	II	0.022797
SN2021T	8657–9101	9.829108	–0.455769	Ia	0.045407

Table A.1 *Countined.*

SN Name	**plate-ifudsgn**	**SN R.A.**	**SN Dec.**	**SN Type**	**redshift**
SDSS-II-SN-12882	8154–9102	45.958199	–0.203996	II	0.027592
SN2020ksa	8993–12701	164.866455	46.124577	Ib	0.022165
SN2016acq	9509–12703	124.102455	25.993111	II	0.045242
SN2016gkm	9501–12705	130.721100	25.070923	Ib	0.017257
SN2003an	8984–9101	201.973129	28.508112	Ia	0.036994
SN2020fcx	8311–12703	205.041748	23.341530	II	0.031926
SN2007O	9033–12705	224.021576	45.404694	Ia	0.036187
PTF11go	8996–6102	173.001007	53.710583	II	0.026810
SN2021bqv	9038–6101	238.758133	41.578018	Ia	0.033563
PTF11cao	9048–12704	244.699829	25.187916	Ia	0.039508
SN2020uoo	9095-6102	243.442657	22.919676	Ia	0.031916
SN2002G	8323–6101	196.980255	34.085140	Ia	0.033650
SN2020ofw	9863–12701	195.139450	27.504499	II	0.018608
SN2009L	9876–12703	194.700424	27.673779	Ia	0.027962
SN2021apg	9881–12704	205.330185	24.495543	II	0.026856
SN2018lev	9871–12702	228.284042	41.263699	II	0.029064
PTF12ewk	9869–12702	247.241119	39.319721	Ia	0.033924
SN2006cq	8322–12705	201.104584	30.956306	Ia	0.048502
SN2020kte	9186–6102	259.121674	29.445555	Ia	0.030187
SN2018emi	9893–9102	256.651367	24.545319	Ia	0.038230
PTF13dfa	8097–6104	27.377167	13.992556	Ia	0.068000
SN2019vin	9189–12705	52.705372	-7.046347	Ia	0.038909
SN2019smi	8986–6101	119.868462	26.889795	Ic	0.026470
SN2020umy	8986–6104	119.902893	28.863256	II	0.045626
SN2006te	10213–12705	122.929123	41.554668	Ia	0.031548
SN2007kd	8152–12701	141.491714	34.633141	Ia	0.024224
SN2012cq	8245–12701	137.022751	20.503471	II	0.025612
SN2019dfa	8438–12702	149.749191	17.818794	Ia	0.025439
SN2016aak	8248–12705	138.554214	16.741722	Ia	0.027855
SN2020hgg	8988–9102	187.235001	40.847279	Ia	0.064948
SN2020fc	10519–12704	154.897339	6.328467	II	0.028476
SN2019vsi	9882–12701	206.479034	23.061930	Ib	0.027886
SN2019hjl	10503–6104	160.622864	5.083230	II	0.028108
SN2012O	9880–12701	195.166626	27.923445	Ia	0.025087
SN2011ki	9040–12701	242.626923	27.499777	II	0.031851
SN2021dxo	8260–6101	182.411789	42.008957	II	0.022881
SN2018ds	8441–12701	222.223206	38.767693	Ia	0.031662
SN2019lpd	9030–9102	243.570999	30.999445	Ia	0.061721
SN1999df	8593–6104	227.235504	52.448082	II	0.037914
SN2001it	8593–12704	226.539169	53.411556	II	0.034190
SN2007ac	11945–12701	251.759827	40.146557	II	0.030193
SN2020ytg	9191–6101	312.041656	-1.211139	II	0.056335
SN2013ag	11871–6102	192.895920	26.629278	Ia	0.021295
SN2012ee	9187–9101	311.313660	-5.622806	Ia	0.027326
LSQ12btw	10518–3703	152.620087	5.536800	Ib	0.057650
SN2006bz	11006–12704	195.180756	27.961611	Ia	0.028093
SN2019gmh	11941–12705	247.763168	41.153965	II	0.030194
SN1992ap	11941–12704	247.613876	41.487804	Ia	0.029864
iPTF13bld	11942–12701	246.227448	41.049789	II	0.033074
SN2009fv	11942–12705	247.434250	40.811611	Ia	0.029338
SN2008cw	11942–6102	248.159454	41.459221	II	0.032433
SN2014bo	11942–12703	246.942291	41.739918	Ia	0.133471
SN2008Z	11751–12703	145.813538	36.284416	Ia	0.020621
SN2020gac	11755–3703	187.442627	42.732700	II	0.038634
PTF11bnf	8563–12701	241.186752	49.457832	Ia	0.024164
SN1940C	8589–12705	226.729172	56.508888	II	0.029552
SN2019qsc	8589–6104	226.512772	55.573055	Ia	0.029223
PTF10bhu	11761–9101	193.868500	53.574638	Ic	0.035834
SNF20080322-000	11979–12704	252.089371	23.614750	Ia	0.030252
SN2001dy	11984–6103	256.247589	23.168388	II	0.030081
SN2010ed	11984–12704	257.350555	22.213362	Ia	0.048984
SN2019gvw	11827–12702	211.810120	49.093830	Ia	0.071327
SN2016acx	11014–1902	194.854996	27.740101	Ia	0.020117
SN2018iun	11018–3703	197.128494	50.641460	II	0.029314
SN2007F	11018–12704	195.812836	50.618805	Ia	0.023619

Balogh, M. L., Morris, S. L., Yee, H. K. C., et al. 1999, ApJ, 527, 54

Barbon, R., Buondí, V., Cappellaro, E., & Turatto, M. 1999, A&AS, 139, 531

Barbon, R., Ciatti, F., & Rosino, L. 1979, A&A, 72, 287

Becker, S. A., & Iben, I., J. 1980, ApJ, 237, 111

Belfiore, F., Westfall, K. B., Schaefer, A., et al. 2019, AJ, 158, 160

Bethe, H. A., Brown, G. E., Applegate, J., & Lattimer, J. M. 1979, Nucl. Phys. A, 324, 487

Blanton, M. R., Bershady, M. A., Abolfathi, B., et al. 2017, AJ, 154, 28

Brinchmann, J., Charlot, S., White, S. D. M., et al. 2004, MNRAS, 351, 1151

Bundy, K., Bershady, M. A., Law, D. R., et al. 2015, ApJ, 798, 7

Cappellari, M., & Emsellem, E. 2004, PASP, 116, 138

Domínguez Sánchez, H., Huertas-Company, M., Bernardi, M., et al. 2018, MNRAS, 476, 3661

Dopita, M. A., Kewley, L. J., Sutherland, R. S., & Nicholls, D. C. 2016, Ap&SS, 361, 61

Dopita, M. A., Sutherland, R. S., Nicholls, D. C., et al. 2013, ApJS, 208, 10

Drory, N., MacDonald, N., Bershady, M. A., et al. 2015, AJ, 149, 77

Fall, S. M., & Efstathiou, G. 1980, MNRAS, 193, 189

Filippenko, A. V. 1997, ARA&A, 35, 309

Fischer, J. L., Domínguez Sánchez, H., & Bernardi, M. 2019, MNRAS, 483, 2057

Gal-Yam, A., Cenko, S. B., Fox, D. W., et al. 2004, in American Astronomical Society Meeting Abstracts, 205, 40.06

Galbany, L., Miquel, R., Östman, L., et al. 2012, ApJ, 755, 125

Galbany, L., Stanishev, V., Mourão, A. M., et al. 2014, A&A, 572, A38

Galbany, L., Stanishev, V., Mourão, A. M., et al. 2016, A&A, 591, A48

Galbany, L., Anderson, J. P., Sánchez, S. F., et al. 2018, ApJ, 855, 107

Gallagher, J. S., Garnavich, P. M., Berlind, P., et al. 2005, ApJ, 634, 210

Goddard, D., Thomas, D., Maraston, C., et al. 2017, MNRAS, 465, 688

Guillochon, J., Parrent, J., Kelley, L. Z., & Margutti, R. 2017, ApJ, 835, 64

Gunn, J. E., Siegmund, W. A., Mannery, E. J., et al. 2006, AJ, 131, 2332

Hamuy, M., Phillips, M. M., Maza, J., et al. 1995, AJ, 109, 1

Hamuy, M., Trager, S. C., Pinto, P. A., et al. 2000, AJ, 120, 1479

Hamuy, M., Maza, J., Pinto, P. A., et al. 2002, AJ, 124, 417

Hoyle, F., & Fowler, W. A. 1960, ApJ, 132, 565

Kashino, D., Renzini, A., Silverman, J. D., & Daddi, E. 2016, ApJL, 823, L24

Kauffmann, G., Heckman, T. M., White, S. D. M., et al. 2003, MNRAS, 341, 33

Kewley, L. J., & Dopita, M. A. 2002, ApJS, 142, 35

Law, D. R., Cherinka, B., Yan, R., et al. 2016, AJ, 152, 83

Mannucci, F., Della Valle, M., Panagia, N., et al. 2005, A&A, 433, 807

Matheson, T., Kirshner, R. P., Challis, P., et al. 2008, AJ, 135, 1598

Mo, H. J., Mao, S., & White, S. D. M. 1998, MNRAS, 295, 319

Perlmutter, S., Aldering, G., Goldhaber, G., et al. 1999, ApJ, 517, 565

Riess, A. G., Filippenko, A. V., Challis, P., et al. 1998, AJ, 116, 1009

Rubin, A., Gal-Yam, A., De Cia, A., et al. 2016, ApJ, 820, 33

Schaefer, A. L., Tremonti, C., Belfiore, F., et al. 2020, ApJL, 890, L3

Sérsic, J. L. 1963, Boletin de la Asociacion Argentina de Astronomia La Plata Argentina, 6, 41

Sersic, J. L. 1968, Atlas de Galaxias Australes

Shao, X., Liang, Y. C., Dennefeld, M., et al. 2014, ApJ, 791, 57

Silverman, J. M., Foley, R. J., Filippenko, A. V., et al. 2012, MNRAS, 425, 1789

Smee, S. A., Gunn, J. E., Uomoto, A., et al. 2013, AJ, 146, 32

Somerville, R. S., Barden, M., Rix, H.-W., et al. 2008, ApJ, 672, 776

Stanishev, V., Rodrigues, M., Mourão, A., & Flores, H. 2012, A&A, 545, A58

Sullivan, M., Conley, A., Howell, D. A., et al. 2010, MNRAS, 406, 782

Thomas, D., Maraston, C., Schawinski, K., et al. 2010, MNRAS, 404, 1775

Westfall, K. B., Cappellari, M., Bershady, M. A., et al. 2019, AJ, 158, 231

Willett, K. W., Lintott, C. J., Bamford, S. P., et al. 2013, MNRAS, 435, 2835

Worthey, G. 1994, ApJS, 95, 107

Yan, R., Bundy, K., Law, D. R., et al. 2016, AJ, 152, 197

Yan, R., Chen, Y., Lazarz, D., et al. 2019, ApJ, 883, 175

Yaron, O., & Gal-Yam, A. 2012, PASP, 124, 668

Zhou, L., Liang, Y.-C., Ge, J.-Q., et al. 2019, RAA (Research in Astronomy and Astrophysics), 19, 121

Zhou, L., Liang, Y.-C., Ge, J.-Q., et al. 2020, RAA (Research in Astronomy and Astrophysics), 20, 169

Zieliński, P., Wyrzykowski, Ł., Rybicki, K., et al. 2019, Contributions of the Astronomical Observatory Skalnate Pleso, 49, 125